


Internal-multiport-model-based fast inverse design of an antireflective artificial metastructure in a waveguide system

Junjie Shao,¹ Ren Wang^{1,*}, Yu Wang,² and Bing-Zhong Wang¹

¹*Institute of Applied Physics, University of Electronic Science and Technology of China, Chengdu 611731, China*

²*Optoelectronics Research Centre, University of Southampton, Highfield, Southampton SO17 1BJ, United Kingdom*

 (Received 11 December 2023; revised 25 March 2024; accepted 3 May 2024; published 28 May 2024)

In practical applications, achieving perfect transmission of electromagnetic waves despite reflections from a complex medium segment in waveguide systems is of great significance. Using a preinstalled antireflective artificial metastructure (ARAMS) to mitigate reflections caused by the presence of a complex medium is an effective solution. The inverse design of ARAMS in waveguide systems is an optimization process. Recent applications of the topology optimization method in designing ARAMS have demonstrated attractive performances [Nature **607**, 281 (2022)]. Topology optimization necessitates frequent utilization of full-wave electromagnetic simulations, while designing from scratch for different functional devices incurs exceedingly high computational costs. To address this problem, we introduce a fast inverse design method for ARAMS based on the internal multiport model (IMPM). Based on a single full-wave electromagnetic simulation dataset, IMPM abstracts the ARAMS electromagnetic field model into a microwave network, analytically establishing connections between actual excitation ports and fictitious internal ports while greatly reducing computational costs in optimization design. Furthermore, once IMPM is established, it can be reused for the rapid optimization design of various functional ARAMS devices in the same complex medium-filled waveguide environment. The cases presented in the paper validate the efficiency of this method in providing effective solutions for the perfect transmission of electromagnetic waves in waveguide systems filled with complex medium.

DOI: [10.1103/PhysRevApplied.21.054055](https://doi.org/10.1103/PhysRevApplied.21.054055)

I. INTRODUCTION

Reducing reflections caused by the presence of a complex medium in waveguide systems is a prominent issue in the field of microwaves [1]. To address this issue, techniques such as the mode-selective technique (MST) [2–4] are proposed for perfect transmission with specific mode channels, providing precise control over the phase and amplitude of propagating waves. However, MST is reliant on the complex medium itself, requiring substantial time investment to find specific mode channels within the medium. Furthermore, for practical applications, structures designed to achieve perfect transmission for one or a few specific mode incidents to a waveguide containing complex medium are inadequate. Recently, a concept was proposed to achieve perfect transmission by placing an antireflective artificial metastructure (ARAMS) in front of the original one to mitigate reflections or scattering losses and verified through an inverse design of the ARAMS within the waveguide system [5]. Nevertheless, the design of the ARAMS proposed in Ref. [5]

is based on topology optimization [6–8], involving the adjustment of material distribution or structure to optimize the electromagnetic wave-propagation characteristics. The space of solutions is vast, requiring frequent utilization of full-wave simulations to assess the fulfillment of design objectives. Additionally, the necessity for creating designs from scratch for ARAMS with various functions results in significant computational expenses and limited model reusability, rendering direct application to different problems a challenging endeavor. In recent years, the continuous development of neural networks appears to offer a potential solution for addressing this problem [9–11]. Neural networks are employed to establish a mapping between optimization variables and design objectives, enabling the fast inverse design of structures in accordance with diverse objectives once established. Moreover, neural networks exhibit strong generalization capabilities, making them applicable to diverse problems within a specific range. However, neural networks prior to the establishment of mapping require a substantial amount of training sample data obtained from full-wave simulations, resulting in high data-collection costs and lengthy network training times. The training process also entails continuous parameter

*Corresponding author: rwang@uestc.edu.cn

adjustments to prevent over- and underfitting, which complicates direct application to structural design and makes the design process more complex and time consuming.

Hence, the challenge of fast designing ARAMS to facilitate antireflective propagation of incident waves with different modes through complex medium-filled waveguide systems, and achieving perfect transmission with various functions [12–15], to satisfy the potential demands in diverse waveguide systems across multiple fields has arisen as a crucial concern [16–20]. To address this question, we propose a fast design method for ARAMS by combining the internal multiport model (IMPM) with optimization algorithms. Internal multiport model, stemming from the internal multiport method, were introduced in the paper [21] and have found extensive applications in pixel antenna design [22,23]. However, the design degrees of freedom and structural variability in existing pixel antenna cases are limited because only the connection states between two-dimensional pixel patches can be configurable, which is insufficient to design ARAMS. In this paper, IMPM is expanded by removing the constraints associated with the connection of internal ports to pixel patches, thereby broadening the design flexibility and enhancing structural adaptability. Strategically arranging several internal ports within the optimization domain and utilizing data acquired from a single full-wave simulation dataset, IMPM abstracts the full-wave electromagnetic model into a microwave network model, analytically establishing the connections between actual excitation ports and fictitious internal ports, leading to a significant reduction in computational costs. By optimizing the state of auxiliary discrete port, the design of ARAMS can be obtained, avoiding the substantial computational expenses associated with establishing mapping using neural networks. Furthermore, the established IMPM can be reused for the fast optimization design of ARAMS within the same complex medium-filled waveguide environment, allowing for the design of ARAMS with diverse functions by simply modifying the objective functions constructed based on the corresponding microwave network port parameters.

II. METHODOLOGY

The design concept schematic of ARAMS is depicted in Fig. 1. A waveguide system filled with a segment of complex medium, representing a complex electromagnetic propagation environment, serves as the demonstration for the inverse design method proposed in this paper. The waveguide is divided into two regions: the optimization region and the region filled with a complex medium, as illustrated in Fig. 1(a). The presence of numerous metallic and dielectric scatterers within the complex medium in

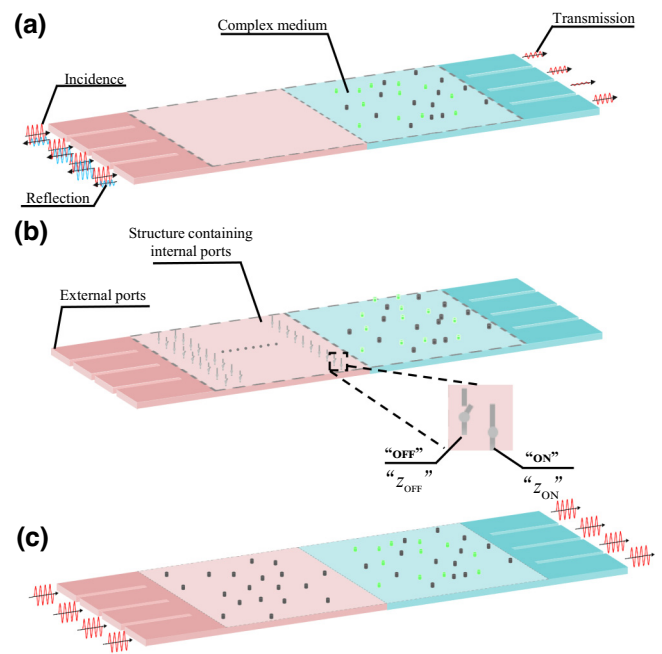


FIG. 1. Design concept schematic of ARAMS. (a) Electromagnetic waves are partially reflected by the complex medium; (b) a preconfigured structure containing internal ports; (c) functional schematic of ARAMS based on the proposed fast inverse design method.

waveguide systems leads to electromagnetic wave scattering, resulting in only a small fraction of the power being able to propagate to the intended destination. In the complex domain of Fig. 1(a), the black cylinders and green cylinders represent the presence of metallic scatterers and dielectric scatterers in the complex waveguide electromagnetic environment. The left side of the complex medium represents the transmitting port, while the right side serves as the receiving port.

To achieve perfect transmission, ARAMS is placed in front of the complex medium to mitigate the complex scattering. Initially, a preconfigured structure with auxiliary discrete ports is positioned in front of the complex medium, as shown in Fig. 1(b). The transmitting and receiving ports, considered as actual excitation ports in this method, are treated as external ports, while the auxiliary discrete ports in the preconfigured structure are regarded as internal ports, with the internal ports having only two states: short circuited and open circuited. In practical devices, the presence or absence of metallic scatterers can represent the two distinct states of internal ports. When metallic scatterers are present, the corresponding internal ports are in a short-circuited state, whereas the absence of metallic scatterers corresponds to an open-circuited state for the respective internal ports at corresponding locations. The ARAMS, with a specific function configured based on the state of an internal multiport, is depicted in Fig. 1(c).

A. Arrangement of internal ports

The internal ports are connected to the upper and lower metal surfaces within the waveguide system, serving to capture field information and transform it into port information. Internal ports at various positions collectively form a microwave network linked to the external excitation (input/output) ports through load conversion of the short-circuited and open-circuited port states. By altering the load states of the multiple ports within the network, the scattering or impedance matrices at the external excitation ports can be modified, achieving optimization objectives, as illustrated in Fig. 2. The arrangement of N auxiliary discrete internal ports, as shown in Fig. 3, combined with the existing W actual excitation ports, forms a microwave network with a total of $W + N$ ports. In Fig. 3, d represents the distance between adjacent internal ports, adjustable as needed. Notably, a small value of $\max\{d\}$ will increase the number of internal ports, offering greater design flexibility but at the cost of higher computational expenses. Conversely, a large value of $\min\{d\}$ will diminish the influence of internal ports on the overall design. In general, the distance between adjacent internal ports is set at around one third of the operating wavelength, which is adequate for capturing the wave-propagation characteristics within the waveguide system and influencing propagation behavior. When faced with challenging optimization objectives, additional internal ports are strategically introduced in the

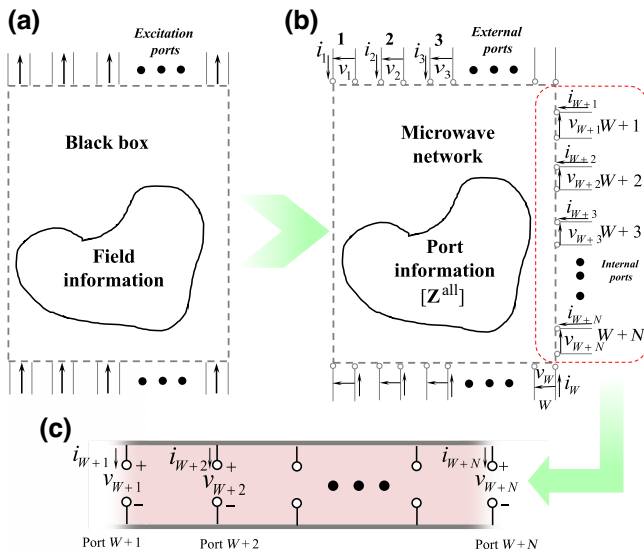


FIG. 2. Diagram of IMPM principle. (a) Physical model of waveguide device with complex media; (b) microwave network model abstracted using IMPM; (c) specific internal multipoint model. “Black box” denotes the cavity area within multipoint devices where the complex medium and field information remain unknown, and port information such as S parameters can only be obtained through ports. The internal ports connected to the upper and lower metal surfaces of the waveguide device.

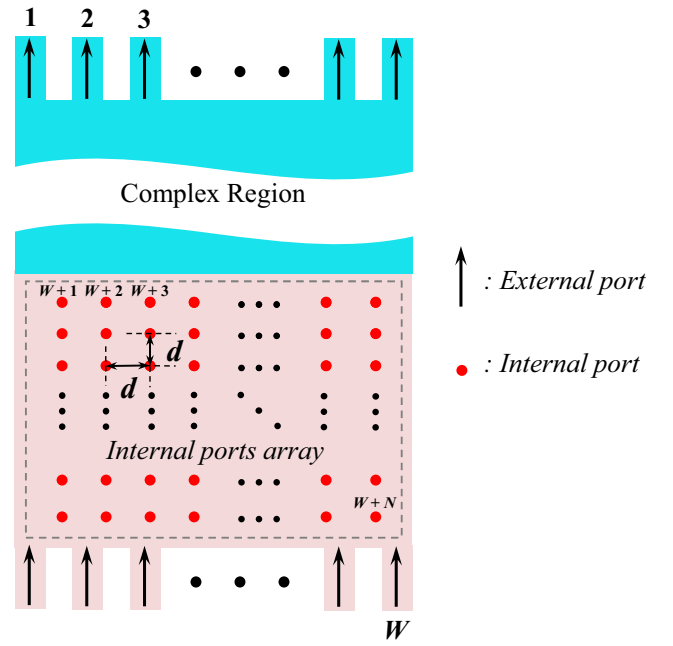


FIG. 3. Schematic arrangement with W external ports and N internal ports. The external ports are numbered 1 to W , and the internal ports are numbered $W + 1$ to $W + N$.

proximity of the internal ports that exhibit a more significant influence on the ARAMS’s performance, thereby enabling the capture of more intricate electromagnetic wave information.

B. Establish IMPM

In the subsequent stage, we need to establish the relationship between the actual excitation ports and the ON and OFF states of the internal ports. Through a sequential excitation of the $W + N$ ports, with the other ports maintained in an open-circuited state using full-wave simulations, we can obtain an impedance matrix encompassing all internal and external ports, as exemplified below:

$$\mathbf{Z}^{\text{all}}(f) = \begin{bmatrix} \mathbf{Z}_{W \times W}^A(f) & \mathbf{Z}_{W \times N}^B(f) \\ \mathbf{Z}_{N \times W}^C(f) & \mathbf{Z}_{N \times N}^D(f) \end{bmatrix} \quad (1)$$

In Eq. (1), W represents the number of external ports, N represents the number of internal ports, $\mathbf{Z}_{W \times W}^A(f)$ represents the impedance submatrix of the external ports; $\mathbf{Z}_{W \times N}^B(f)$ and $\mathbf{Z}_{N \times W}^C(f)$, respectively, represent the transmission impedance between the external ports and the internal ports, and $\mathbf{Z}_{N \times N}^D(f)$ represents the impedance submatrix of the internal ports. $\mathbf{Z}^{\text{all}}(f)$ is frequency related, and to simplify the subsequent derivation, the frequency symbol f has been omitted.

During the design process, the ON or OFF states of the internal ports are considered as load states and can be represented using a set of vectors \mathbf{Z}^L ,

$\mathbf{Z}^L = \{Z_{N+1}^L, Z_{N+2}^L, \dots, Z_{N+W}^L\}$, the element $Z_{N+1}^L, Z_{N+2}^L, \dots, Z_{N+W}^L$ represents the load-impedance values of each internal port, which correspond to the actual electrical characteristics of the internal ports in short-circuited or open-circuited states (respectively, denoted as z_{ON} or z_{OFF}). After loading specific \mathbf{Z}^L onto N ports, the impedance matrix for the current W external ports can be obtained based on IMPM and is expressed as follows:

$$\mathbf{Z}^{\text{act}} = \mathbf{Z}_{W \times W}^A - \mathbf{Z}_{W \times N}^B \times \left(\mathbf{Z}_{N \times N}^D + \mathbf{Z}_{N \times N}^{L'} \right)^{-1} \times \mathbf{Z}_{N \times W}^C$$

$$\mathbf{Z}_{N \times N}^{L'} = \text{diag}(\mathbf{Z}^L), \quad (2)$$

where \mathbf{Z}^{act} represents the impedance matrix of the external ports, $\mathbf{Z}_{N \times N}^{L'}$ represents the diagonal matrix of the load-impedance values for internal ports.

At this juncture, with the impedance matrix for the actual excitation ports successfully established, the corresponding scattering matrix can be obtained by the conversion relationship within the microwave network [24] as follows:

$$\mathbf{S}^{\text{act}} = \mathbf{G}_W^0 \cdot \left(\mathbf{Z}^{\text{act}} - \mathbf{Z}_W^{0*} \right) \cdot \left(\mathbf{Z}^{\text{act}} + \mathbf{Z}_W^0 \right)^{-1} \cdot \left(\mathbf{G}_W^0 \right)^{-1}$$

$$\mathbf{G}_W^0 = \text{diag}(\mathbf{F}_W^0), \quad (3)$$

where $\mathbf{F}_W^0 = \left\{ 1 / \left(2\sqrt{\text{Re}\{Z_1^0\}} \right), 1 / \left(2\sqrt{\text{Re}\{Z_2^0\}} \right), \dots, 1 / \left(2\sqrt{\text{Re}\{Z_W^0\}} \right) \right\}$, $\mathbf{Z}_W^0 = \{Z_1^0, Z_2^0, \dots, Z_W^0\}$, Z_i^0 is the characteristic impedance of the i th external port and \mathbf{S}^{act} is the scattering matrix of actual excitation ports, so the relationship between the scattering matrix and the ON or OFF states of the internal ports has been established.

By utilizing internal ports to capture electromagnetic field information at specific locations and mapping complex field distributions to discrete port parameters, the field information from full-wave simulations is abstracted into port information of microwave network, allowing optimization designs to focus on port interactions without the need to consider intricate field distributions. The transformation of ARAMS optimization designs from reliance on repeated full-wave electromagnetic simulations to microwave network models significantly reduces computational requirements for inverse design, enabling the fast design of ARAMS with specific function within seconds.

C. Correction of IMPM

In IMPM, the load states of internal ports correspond to the optimizable structures within ARAMS. When the optimizable structures of the ARAMS are infinitely fine metal segments, z_{ON} and z_{OFF} are set to “ 0Ω ” and “ ∞ ,” respectively, indicating the presence and absence of short-circuited metallic cylinders at the corresponding position.

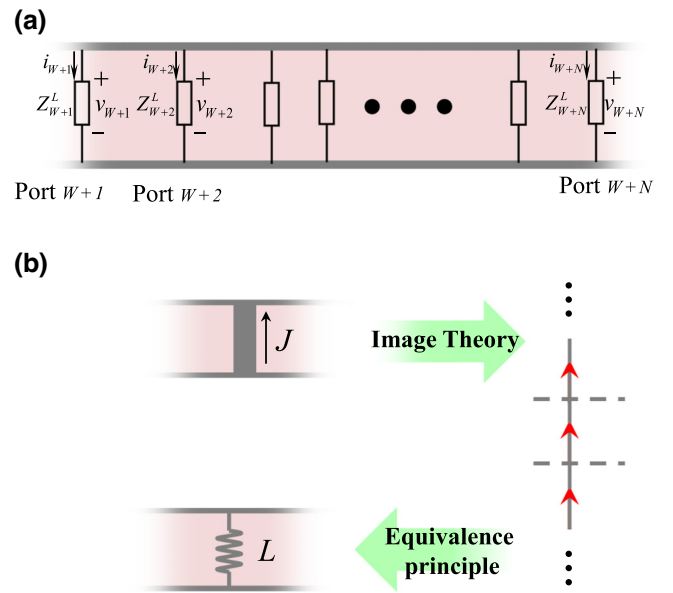


FIG. 4. Equivalent circuit diagram. (a) Equivalent circuit model of N internal ports with load impedance \mathbf{Z}^L ; (b) equivalent principle for internal port short-circuit state.

However, in practice, due to manufacturing constraints, the optimizable structures are not infinitely fine. This implies that the impedance of the internal port's connected state is not 0Ω , and the reactive effects in the short-circuited state of the internal ports must be considered. A simplified scenario is considered in this paper, where the length of the short-circuited metallic cylinder is chosen to be one fifteenth of the operating wavelength, and the radius is much smaller than the operating wavelength. The induced current on the metallic cylinder is assumed to remain basically constant, as shown in Fig. 4(b). Applying the principle of image theory, the induced current on the metallic cylinder can be equivalent to an infinitely long current source. By calculating the unit-length equivalent inductance, the equivalent inductance of the metallic cylinder at that radius can be determined, allowing for corrections in the short-circuited state.

It is worth mentioning that once the port impedance values in the short-circuited state are determined, within the same design framework, these values are applicable to all subsequent optimization designs.

D. Optimization

IMPM transforms the electromagnetic inverse design problem into a numerical optimization task with two variable states by linking the S parameters of actual excitation ports to the internal port ON or OFF states, enabling the application of various optimization algorithms [25–29]. Genetic algorithm (GA), as one of the representatives of classical optimization algorithms, is used to realize the

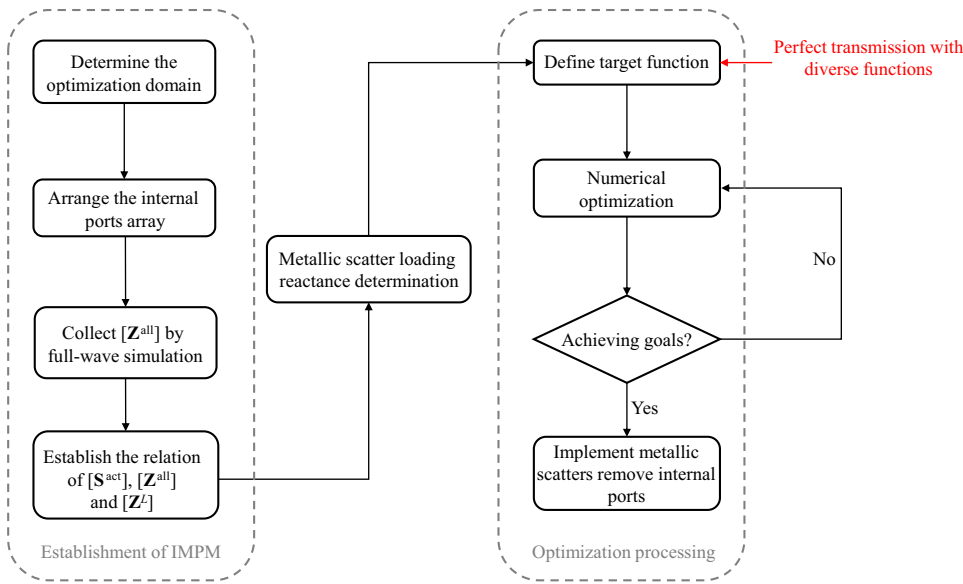


FIG. 5. Flowchart of the proposed inverse design method. The overall design process of ARAMS involves two main stages: establishing IMPM and optimizing the design. Once IMPM is established, maintaining the optimization domain, ARAMS can be fast designed for the same complex medium with different functions.

fast design of ARAMS in this paper. The load states of N internal ports are represented by a binary vector $\mathbf{x} = \{x_1, x_2, x_3, \dots, x_N\}$, where $x_i = 0$ or 1 represents the i th internal port is short- or open-circuited states, respectively. Using GA to optimize binary vectors, the ARAMS design

that meets the design objectives is completed by placing metallic scatters at the short-circuited internal ports.

Figure 5 illustrates an optimization process for improved clarity. The process begins with establishing the corresponding model framework based on the complex

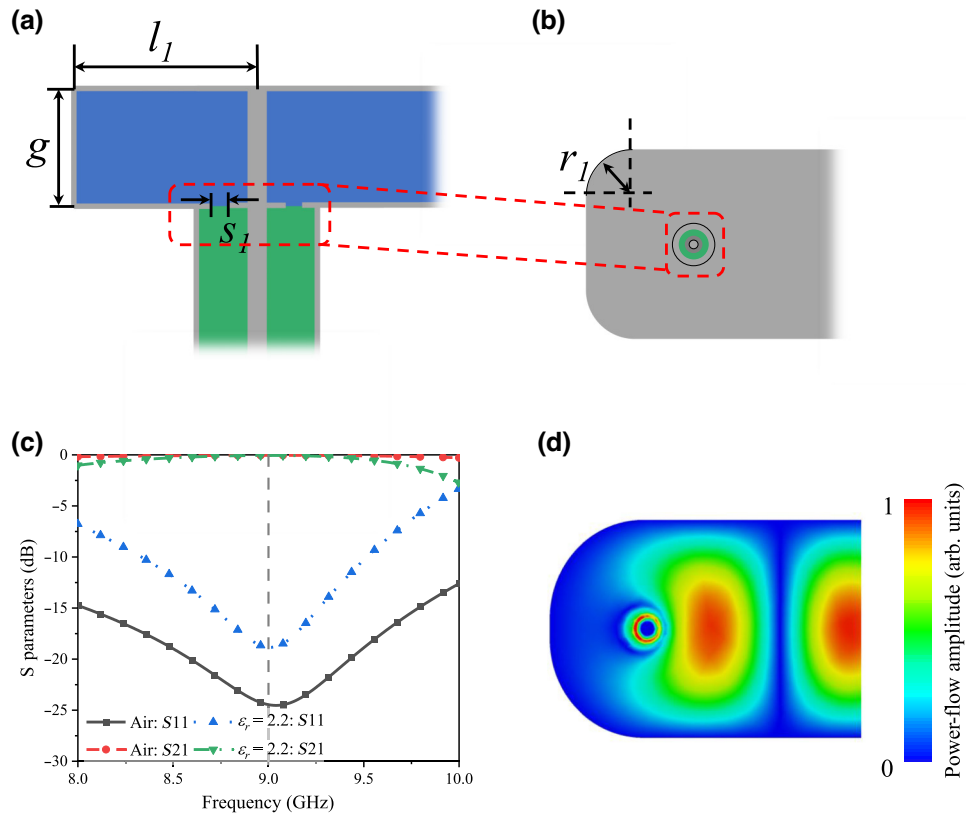


FIG. 6. Diagram of coaxial waveguide converter. (a) Side view; (b) top view; (c) optimized S parameters under different background materials; (d) electric field based on a substrate with a dielectric constant of 2.2 at 9 GHz. (ϵ_r represents the relative dielectric constant of the substrate.)

medium, followed by determining the arrangement of auxiliary discrete ports. Subsequently, initial impedance data is obtained through full-wave simulations to capture field information at corresponding positions and presented in the form of S parameters. Corrections are then made to the load impedance under the given ON or OFF state. After defining the objective function, numerical optimization using GA yields a set of 0–1 distributions indicating whether metallic scatterers are placed at corresponding positions. Completing the ARAMS design involves replacing internal ports at corresponding positions with metallic scatterers. By adjusting different objective functions, diverse configurations of metallic scatterers can be achieved, facilitating rapid inverse design of ARAMS with various functionalities without reacquiring the initial impedance matrix data.

III. DEMONSTRATION OF PERFECT TRANSMISSION FOR VARIOUS INPUTS

In this study, we employed the proposed method to design several cases, consistently achieving excellent performance. Due to space constraints, this section demonstrating perfect transmission for various inputs using ARAMS. This case is chosen as it presents a more

challenging design objective in comparison to other targets. Different transmitting ports may require operation at distinct times, necessitating the ARAMS design to ensure individual perfect transmission for each port. Consequently, the ARAMS design is required to meet these rigorous demands for each port.

A. Simulation

An eight-port over-mode rectangular waveguide with dimensions of $220 \times 100 \times 1 \text{ mm}^3$ is selected as carrier, operating at a frequency of 9 GHz, where ports 1–4 served as transmitters, and ports 5–8 as receivers.

Ports 1 to 8 correspond to the coaxial waveguide converters operating in the dominant mode, with the specific structures depicted in Fig. 6. Here, “ g ” represents the waveguide height, “ l_1 ” indicates the distance from the probe position to the waveguide reflective wall, “ s_1 ” denotes the distance between two matching loops at different positions, and “ r_1 ” signifies the degree of circular chamfering of the rectangular waveguide reflection cavity. For achieving better impedance matching and signal transmission efficiency, a matching loop was added at the connection point between the coaxial probe and the waveguide to reduce reflection and loss at the target frequency,

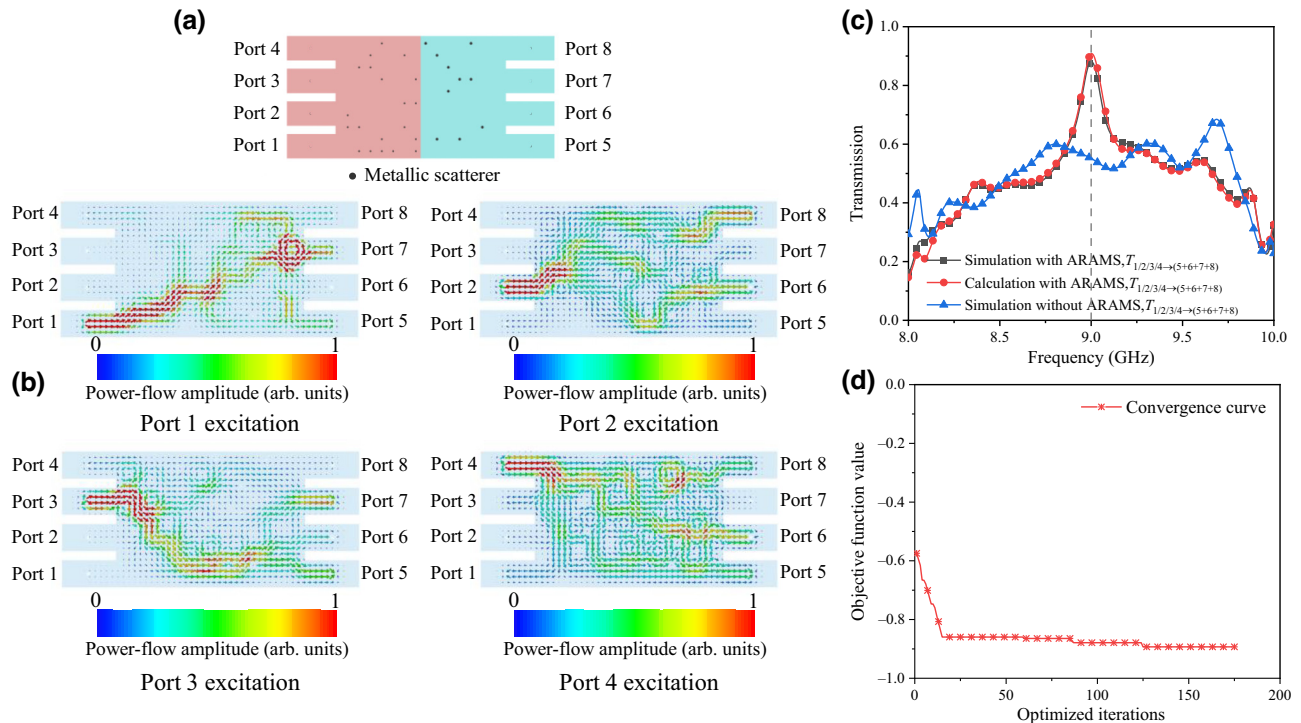


FIG. 7. Function of perfect transmission for various inputs. (a) ARAMS loaded structures; (b) power-flow diagram with ARAMS of each excited port; (c) power-transmission coefficient; (d) convergence curve of the optimization. (Simulation with ARAMS represents the simulation results of the device with ARAMS, while simulation without ARAMS represents the results without ARAMS. Calculation with ARAMS represents the result of the numerical calculation with ARAMS, T represents the average normalized power-transmission coefficient, the left side of the arrow is the excitation port, the right side indicates the receiving port, “/” indicates “or excitation”).

as shown in Figs. 6(a) and 6(b). Optimization simulations revealed that, without altering the height of the rectangular waveguide, the distance between the coaxial probe and the waveguide's reflective wall, the positioning and size of the matching ring, and the degree of chamfering of the rectangular waveguide's reflective cavity significantly affect the matching between the coaxial and rectangular waveguides. By adjusting these parameters, optimal transmission performance at 9 GHz with different background materials can be achieved. The corresponding S parameters and electric field diagrams are depicted in Figs. 6(c) and 6(d).

Multiple metallic scatterers, each with a 1-mm radius, were added within the disordered region shown in the blue area of Fig. 7(a) to replicate a complex electromagnetic environment. Within the optimization region, 10×7 discrete ports are arranged (with the minimum separation distance for auxiliary discrete ports set at $\lambda/3$ according to Sec. II), using 0.3-mm diameter metallic scatterers to represent the auxiliary discrete ports in the short-circuited state.

The optimization problem can be formulated as

$$\begin{aligned} \min_{\mathbf{x}} & -\frac{1}{4} \sum_{i=5}^8 \sum_{j=1}^4 |S_{ij}(\mathbf{x}, f)|^2 \\ \text{such that } & \mathbf{x} \in \{0, 1\}^N \\ & f = 9 \text{ GHz}. \end{aligned} \quad (4)$$

Complete impedance matrix data can be collected using the CST full-wave simulation software on a computer with an Intel(R) Core(TM) i7-7700K CPU @ 4.2 GHz in 0.78 h. Following the data collection, an optimization process for the ON or OFF states of internal ports, based on the objective function and in accordance with the steps outlined in Sec. II, is carried out using GA with a population size of 60, a crossover rate of 0.8, and a mutation rate of 0.8. Convergence of the optimization is achieved after a hundred iterations. Subsequently, the short-circuited states of internal ports are replaced with metallic scatterers, followed by full-wave simulations.

As shown in Fig. 7(b), when individually exciting ports 1–4, electromagnetic waves transmit through the ARAMS and complex medium, with power almost entirely directed toward the receiving port, exhibiting minimal reflection. For a more straightforward comparison of power reception efficiencies between loaded and unloaded ARAMS scenarios, an average normalized power coefficient labeled T is introduced.

$$T = \frac{1}{n} \left(\sum_j |t_j|^2 \right), t_j = \sum_i S_{ji}, \quad (5)$$

$i \in \{1, 2, 3, 4\}, j \in \{5, 6, 7, 8\}$,

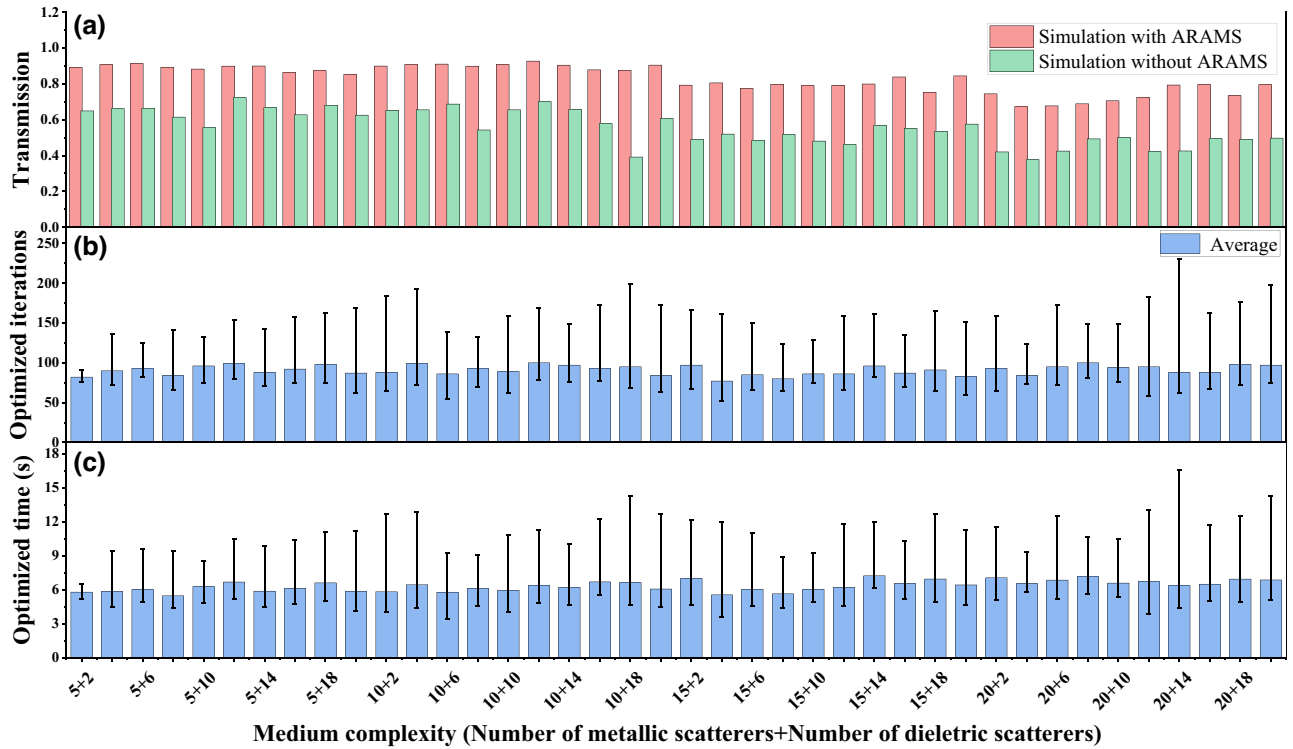


FIG. 8. Comparison of perfect transmission for various inputs with different complex medium. (a) Power-transmission coefficients. (b) Number of optimization iterations. (c) Optimization time. (The error bars represent the maximum and minimum values of the optimization iterations and time for designing ARAMS through multiple optimizations at the corresponding complexity of complex medium.)

where i and j denote the excitation and the receiving port labels, respectively, n denotes the number of selected excitation ports, t_j denotes the superposition of the S parameter from each excitation port to the j th receiving port, and T denotes the average normalized power-transmission coefficient.

The results contained full-wave simulation and numerical computation for T are summarized in Fig. 7(c). Compared to the scenario where ARAMS is not prepositioned in the complex medium, T significantly increased from 55% to 90%, demonstrating the achievement of this function and confirming the feasibility of the proposed method.

To mitigate the randomness associated with single optimization instances, we performed 20 optimizations with various metallic and dielectric scatterers mixed in complex media, using air as the background material, while maintaining the same design objectives as those stated in the text. The statistical results are depicted in Fig. 8. The figure depicts the complexity of diverse complex medium based on various combinations of metallic and dielectric scatterers, with the number of metallic scatterers as the primary determinant and dielectric scatterers as secondary factors.

As illustrated in Fig. 8(a), as the complexity of the medium increases, so does the difficulty of optimization. However, by deploying ARAMS optimization prior to the complex medium, improvements in transmission efficiency were achieved across all complex medium under 20 optimizations. Furthermore, optimization of ARAMS for different complexity of the complex medium converged within 250 iterations, with times consistently under 18 s.

B. Experimental verification

Following the case discussed in Sec. III A, ARAMS designed to achieve perfect transmission with various inputs was fabricated and measured based on a dielectric substrate with a dielectric constant of 2.2, a loss angle tangent of 0.001, and a thickness of 1.5 mm.

The structures loaded ARAMS and corresponding photographs are presented in Fig. 9, where Area 1 represents the optimized area with 0.3-mm diameter metallized holes to simulate the metallic scatterers, and Area 2 represents the complex medium area with a 1-mm diameter metallized hole to simulate the complex medium. The fabricated structures were measured and compared with simulation

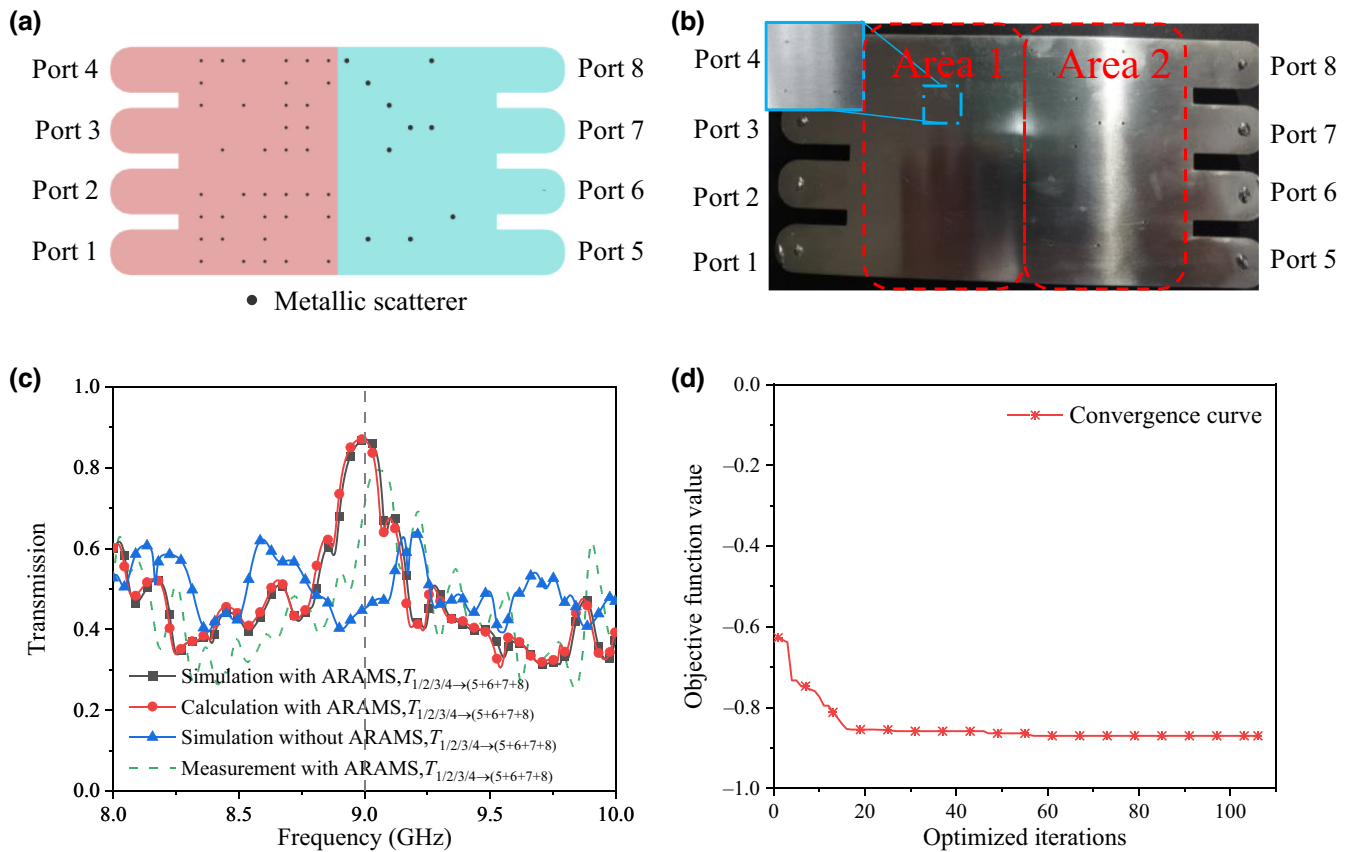


FIG. 9. Function of perfect transmission for various inputs. (a) Simulation model of ARAMS-loaded structures; (b) photographs of the fabrication of the ARAMS loading structure; (c) comparison of simulation, calculation, and measurement of power-transmission coefficients; (d) optimized convergence diagram. (Measurement with ARAMS represents the measurement with the ARAMS.)

and calculation results, as shown in Fig. 9. The rectangular structures with semicircles in Figs. 9(a) and 9(b) represent coaxial rectangular waveguide configurations, ensuring the operation of the small waveguide in the dominant mode.

While the dielectric substrate loss and machining error lead to some discrepancies between the measurement and simulation results, the overall trend of the curves is consistent, and the average normalized power-transmission coefficient is significantly improved compared to the case of unloaded ARAMS, further validating the effectiveness of the proposed method.

C. Discussion

1. Comparison

Topology optimization achieves optimal performance of electromagnetic devices by adjusting parameters, such as geometric shapes and material distributions to meet the objective function, but necessitates continuous full-wave simulations during the iterative optimization process to assess its impact on device performance. Moreover, with changing optimization objectives, topology optimization often requires extensive repetition of full-wave simulations, lacking reusability and incurring high time costs.

The IMPM model established after obtaining the initial matrix allows for reuse without altering the optimization region or complex medium. The ARAMS with the function of single-input single-output perfect focusing transmission is designed based on the initial matrix for perfect transmission for various inputs aforementioned, and the objective function is defined as

$$\begin{aligned} \min_{\mathbf{x}} \quad & -|S_{73}(\mathbf{x}, f)|^2 \\ \text{such that} \quad & \mathbf{x} \in \{0, 1\}^N \\ & f = 9 \text{ GHz.} \end{aligned} \quad (6)$$

For this case, the transmission coefficient is defined as the power transmitted from port 3 output to port 7. After integrating ARAMS, the transmission coefficient increased from 31.2% to 95.6% as shown in Fig. 10, allowing for diverse functions within the same complex medium and validating the reusability of the method proposed in this paper.

The data-driven neural network, though theoretically reusable, necessitates collecting a large amount of data to fit the relationship between internal port ON or OFF states and S parameters. In the case study presented in this paper, the metallic scatterers are deep subwavelength

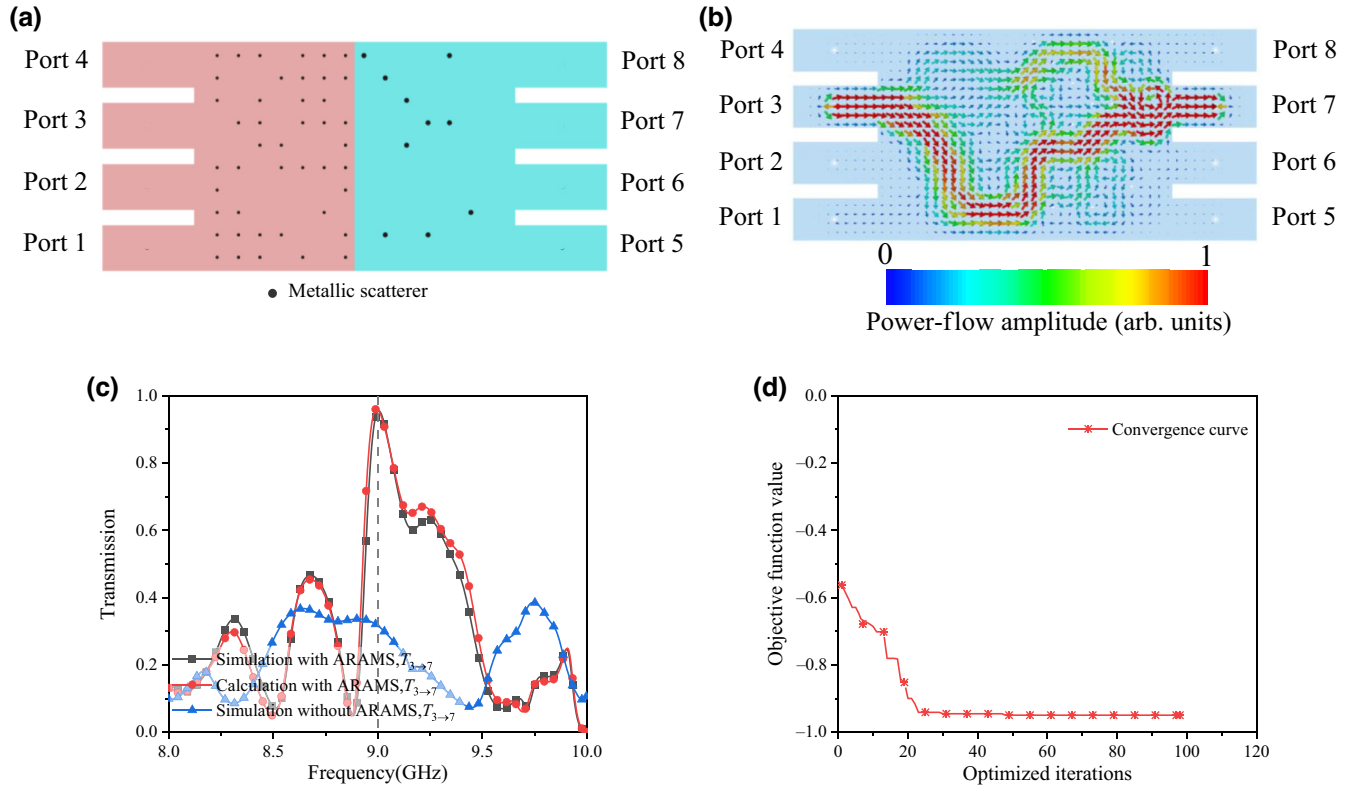


FIG. 10. Function of single-input single-output perfect focusing transmission; (a) simulation model of ARAMS-loaded structures; (b) power-flow diagram with ARAMS of excited port 3; (c) comparison of simulation and calculation of power-transmission coefficients; (d) convergence curve of the optimization.

structures, leading to increased grid counts during full-wave simulations for enhanced accuracy, resulting in a simulation time of 2.12 h for one ON or OFF configuration of internal ports. Due to the 70 optimization variables, the complete set comprises a total of 2^{70} cases. With purely data-driven neural networks requiring 30% to 70% of the total data, the time cost of collecting data amounts to at least approximately 7.08×10^{20} h, which is unacceptable. The method proposed in this paper employed for data collection during full-wave simulations involves setting internal ports as discrete excitation sources in the full-wave simulation software, thereby avoiding the need for fine-grid partitioning and mitigating computational load compared to simulations with specific metallic scatterer structures. Additionally, this method has established an analytical relationship between internal port ON or OFF states and S parameters, obviating the necessity for extensive full-wave simulations to obtain training data for fitting, thus requiring only the complete initial impedance matrix for subsequent optimization, enabling fast ARAMS design.

2. Extension

The internal multiport model is to establish analytically the relationship between optimization variables and S parameter, applicable not only to switching ON or OFF systems. The open and short circuits discussed in this paper represent just two basic states, while the loads applied at the port can encompass various lumped-element models of media. Theoretically, any load that can be equivalently represented by a lumped-element model can be considered as one of the load states, enabling multibit optimization. We will provide a simple example to illustrate this concept as following. Expanding the load states to include 1- and 10-nH inductors, 1- and 10-pF capacitors, along with an open circuit, while keeping the design objective constant, the optimized results are shown in Fig. 11.

With the adoption of additional load states, ARAMS optimization presents more possibilities. Loading the redesigned ARAMS results in a significant enhancement in transmission efficiency compared to the unloaded scenario, thereby demonstrating that this method is not limited solely to switch systems.

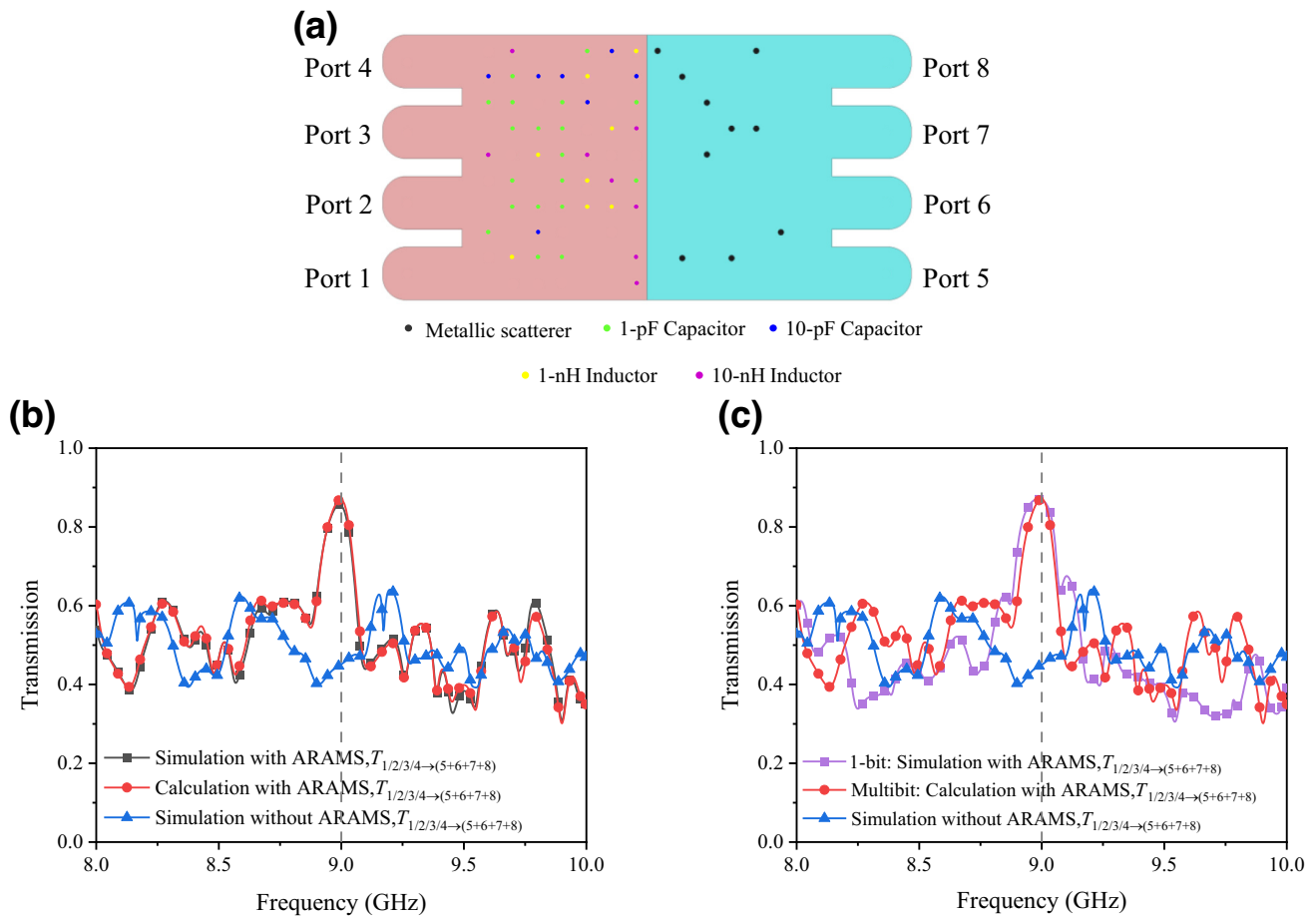


FIG. 11. Function of function of perfect transmission for various inputs with multibit optimization. (a) Simulation model of ARAMS-loaded structures; (b) comparison of simulation and calculation of power-transmission coefficients; (c) comparison of 1-bit and multibit optimization of power-transmission coefficients.

IV. CONCLUSION

We propose an IMPM-based fast inverse design method to design ARAMS. Employing IMPM to abstract the full-wave electromagnetic field model in waveguide systems containing a complex medium into a microwave network model, this method substantially reduces computational costs and enables the efficient design of ARAMS with various functions in a few seconds. Through optimizing the ON or OFF states of internal ports, precise control over the port scattering matrix of the device is achieved, offering greater flexibility for electromagnetic device applications in complex electromagnetic environments. Furthermore, this method is not confined to waveguide systems and can be extended to other electromagnetic systems, offering a fresh perspective to address scattering losses in other environments.

ACKNOWLEDGMENTS

This work was supported in part by the National Natural Science Foundation of China under Grants No. 62171081 and No. U2341207, the Aeronautical Science Foundation of China 2023Z062080002, the Natural Science Foundation of Sichuan Province under Grant No. 2022NSFSC0039.

-
- [1] N. Ha-Van, C. Simovski, F. Cuesta, P. Jayathurathnage, and S. Tretyakov, Effective midrange wireless power transfer with compensated radiation loss, *Phys. Rev. Appl.* **20**, 014044 (2023).
- [2] M. Khatibi Moghaddam and R. Fleury, Subwavelength metawaveguide filters and metaports, *Phys. Rev. Appl.* **16**, 044010 (2021).
- [3] V. K. Killamsetty and A. Epstein, Metagratings for perfect mode conversion in rectangular waveguides: Theory and experiment, *Phys. Rev. Appl.* **16**, 014038 (2021).
- [4] S. W. Lee, S. I. Kim, H. M. Seung, and J. H. Oh, Mode-selective elastic metasurfaces, *Phys. Rev. Appl.* **19**, 014024 (2023).
- [5] M. Horodyski, M. Kühmayer, C. Ferise, S. Rotter, and M. Davy, Anti-reflection structure for perfect transmission through complex media, *Nature* **607**, 281 (2022).
- [6] Z. Lin, B. Groever, F. Capasso, A. W. Rodriguez, and M. Lončar, Topology-optimized multilayered metaoptics, *Phys. Rev. Appl.* **9**, 044030 (2018).
- [7] R. E. Christiansen, F. Wang, and O. Sigmund, Topological insulators by topology optimization, *Phys. Rev. Lett.* **122**, 234502 (2019).
- [8] B. Zhao, D. Wang, P. Zhou, X. Liu, and G. Hu, Design of load-bearing materials for isolation of low-frequency waterborne sound, *Phys. Rev. Appl.* **17**, 034065 (2022).
- [9] M. Matuszewski, A. Opala, R. Mirek, M. Furman, M. Król, K. Tyszka, T. Liew, D. Ballarini, D. Sanvitto, J. Szczytko, and B. Pietka, Energy-efficient neural network inference with microcavity exciton polaritons, *Phys. Rev. Appl.* **16**, 024045 (2021).
- [10] C.-D. Han, B. Glaz, M. Haile, and Y.-C. Lai, Adaptable Hamiltonian neural networks, *Phys. Rev. Res.* **3**, 023156 (2021).
- [11] J. M. Martyn, K. Najafi, and D. Luo, Variational neural-network ansatz for continuum quantum field theory, *Phys. Rev. Lett.* **131**, 081601 (2023).
- [12] K. Zafari and H. Oraizi, Surface waveguide and y splitter enabled by complementary impedance surfaces, *Phys. Rev. Appl.* **13**, 064025 (2020).
- [13] W. Song, T. Li, S. Wu, Z. Wang, C. Chen, Y. Chen, C. Huang, K. Qiu, S. Zhu, Y. Zou, and T. Li, Dispersionless coupling among optical waveguides by artificial gauge field, *Phys. Rev. Lett.* **129**, 053901 (2022).
- [14] Y.-L. Zhao, C. Sheng, Z.-Y. Liu, S.-N. Zhu, and H. Liu, Integrated broadband mode division demultiplexer in waveguide arrays, *Phys. Rev. Appl.* **19**, 064014 (2023).
- [15] S. Khattou, Y. Rezzouk, M. Amrani, M. El Ghafiani, E. H. El Boudouti, A. Talbi, and B. Djafari-Rouhani, Friedrich-Wintgen bound states in the continuum in a photonic and plasmonic T-shaped cavity: Application to filtering and sensing, *Phys. Rev. Appl.* **20**, 044015 (2023).
- [16] K. Zeyde and V. Sharov, in *2018 International Conference on Actual Problems of Electron Devices Engineering (APEDE)* (IEEE, Saratov, Russia, 2018), p. 294.
- [17] B. Orazbayev, N. Kaina, and R. Fleury, Chiral waveguides for robust waveguiding at the deep subwavelength scale, *Phys. Rev. Appl.* **10**, 054069 (2018).
- [18] H. Zhang, H. Chu, H. Giddens, W. Wu, and Y. Hao, Experimental demonstration of Luneburg lens based on hyperuniform disordered media, *Appl. Phys. Lett.* **114**, 053507 (2019).
- [19] M. M. Milošević, W. Man, G. Nahal, P. J. Steinhardt, S. Torquato, P. M. Chaikin, T. Amoah, B. Yu, R. A. Mullen, and M. Florescu, Hyperuniform disordered waveguides and devices for near infrared silicon photonics, *Sci. Rep.* **9**, 20338 (2019).
- [20] R. Li and Y. Hadad, Reduced sensitivity to disorder in a coupled-resonator waveguide with disordered coupling coefficients, *Phys. Rev. A* **103**, 023503 (2021).
- [21] S. C. Song and R. D. Murch, An efficient approach for optimizing frequency reconfigurable pixel antennas using genetic algorithms, *IEEE Trans. Antennas Propag.* **62**, 609 (2014).
- [22] S. Soltani, P. Lotfi, and R. D. Murch, Design and optimization of multipoint pixel antennas, *IEEE Trans. Antennas Propag.* **66**, 2049 (2018).
- [23] M. Li, Y. J. Zhang, D. Wu, K. L. Yeung, L. J. Jiang, and R. Murch, Decoupling and matching network for dual-band MIMO antennas, *IEEE Trans. Antennas Propag.* **70**, 1764 (2022).
- [24] D. M. Pozar, *Microwave Engineering* (Wiley, NY, USA, 2004).
- [25] U. Las Heras, U. Alvarez-Rodriguez, E. Solano, and M. Sanz, Genetic algorithms for digital quantum simulations, *Phys. Rev. Lett.* **116**, 230504 (2016).
- [26] G. Costagliola, R. Guarino, F. Bosia, K. Gkagkas, and N. M. Pugno, Evolutionary algorithm optimization of

- staggered biological or biomimetic composites using the random fuse model, *Phys. Rev. Appl.* **13**, 034049 (2020).
- [27] J. Bowles, A. Dauphin, P. Huembeli, J. Martinez, and A. Acín, Quadratic unconstrained binary optimization via quantum-inspired annealing, *Phys. Rev. Appl.* **18**, 034016 (2022).
- [28] A. B. Magann, K. M. Rudinger, M. D. Grace, and M. Sarovar, Feedback-based quantum optimization, *Phys. Rev. Lett.* **129**, 250502 (2022).
- [29] C. Roy, W. Lin, and K. Wu, Swarm intelligence-homotopy hybrid optimization-based ANN model for tunable band-pass filter, *IEEE Trans. Microw. Theory Techn.* **71**, 2567 (2023).